https://doi.org/10.1016/j.ijhydene.2021.03.192

Numerical study of high temperature proton exchange membrane fuel cell (HT-PEMFC) with a focus on rib design

Lingchao Xia [a], Qidong Xu [a], Qijiao He [a], Meng Ni [a, *], Meng Seng [b]

[a] *Building Energy Research Group, Department of Building and Real Estate, Research Institute for Sustainable Urban Development (RISUD), The Hong Kong Polytechnic University, Hung Hom, Kowloon, Hong Kong, China*

[b] *Clean Energy Research Centre, Duralite Power Pte Ltd, Singapore*

Corresponding author: Email – meng.ni@polyu..edu.hk (M.Ni); Tel: 852-27664152

Abstract

The rib size is a critical engineering design parameter for high temperature proton exchange membrane fuel cell (HT-PEMFC) stack development, yet it hasn't been studied for HT-PEMFC. A three-dimensional, non-isothermal model was developed in this work to investigate the effect of channel to rib width ratios (CRWR) on the performance of HT-PEMFC. The reaction heat caused by entropy change was divided into cathodic half-reaction heat and anodic half-reaction heat. The results show that the ratio value significantly influence the gas diffusion, electron conduction and the distribution of current density in the porous electrodes. Increasing this ratio facilitates gas transport in the porous electrode but causes higher ohmic loss due to longer distance for electron conduction. As a result, an optimal ratio of about 1 is observed, which results in a peak power density of 0.428 W/cm^2. High current density is observed under the channel with a small ratio value while a high ratio value would cause high current density to appear under the rib, signifying the rib size effect on electrochemical

behavior of HT-PEMFC. Apart from the electrical power output, the CRWR value also greatly influences the fluid flow and temperature distribution inside the cell, which would influence the long-term stability of HT-PEMFC. In the subsequent studies, efforts will be made to develop new stack configurations with more uniform gas distribution, short electron conduction path and low temperature gradient.

Key words: HT-PEMFC; Channel to rib width ratio; Reactants distribution; Thermal behavior.

Nomenclature

E	Ideal voltage [V]	η_{ohmic}	Ohmic loss [V]
E^0	Open circuit voltage [V]	η_{conc}	Concentration loss [V]
E_a	Activation energy [J/mol]	η_{act}	Activation loss [V]
T	Operating temperature [°C]	R_{ohmic}	Ohmic resistance [ohm]
$a_{products}^{v_i}$	Product pressure [Pa]	R_{elec}	Electron resistance [ohm]
$a_{reactants}^{v_i}$	Reactant pressure [Pa]	R_{ionic}	Ionic resistance [ohm]
R	Universal gas constant [J/mol/K]	n	Moles [mol]
F	Faraday constant [C/mol]	c_R^0	Reactant concentration in GDL [mol/m^3]
j_0	Exchange current density [A/cm^2]	c_R^*	Reactant concentration in CL [mol/m^3]
j	Current density [A/cm^2]	α	Charge transfer coefficient
i	Current [A]	DL	Doping level of H_3PO_4

u	Velocity [m/s]	ρ	Density [kg/m^3]
Q	Heat generation [J]	μ	Dynamic viscosity [kg/m·s]
λ	Thermal conductivity [W/m·K]	C_p	Heat capacity [J/kg·K]

1. Introduction

Proton exchange membrane fuel cell (PEMFC) is a promising solution to the future power sources due to its high-power density and no pollution. Recently, the high temperature proton exchange membrane fuel cell (HT-PEMFC) is getting more attention because of its simplified water management system[1-4], higher tolerance to carbon monoxide [5-7] and faster reaction kinetics [8, 9] compared with low temperature PEMFC.

Many simulation and experimental works on HT-PEMFC have been carried out over the last decade. Most of them focuses on the materials optimization including membranes [10-12], catalysts layers (CL) [13-15]1and gas diffusion layers (GDL) [16-18], which allows the fuel cell to work under the temperature range of 120 - 200 °C. Besides, a lot of works like study of CO tolerance [19-21], energy system design [22-26], heating [27, 28] and control strategy [29-31] are conducted. Although the flow field design of low temperature PEMFC has been widely studied, the research of this issue on HT-PEMFC is limited.

Regarding the numerical study, Peng et al. [32] developed a 3D model to reveal the fundamental processes taking place in each component of HT-PEMFC and pointed out the cell performance would get affected greatly by the current collector land area. Liu et al. [33] did research on relationship between flow channel design and cell performance. They reported that modified gas distribution improved O_2 supply in the GDL and CL. Lobato et al. [34] built an

isothermal model to numerically evaluate three types of flow channel geometries. Yin et al. [35] reported a greater ohmic loss with the presence of ribs. Drakselová et al. [36] developed a 3D model of industrial-scale cells with different flow field designs and reported that the stack behavior significantly gets affected by the non-uniform distribution of both reactants and current density.

Experimentally, three designs of channel geometries were studied by Rodolfo et al. [37] and the results shows that serpentine geometry yields best performance. Tseng et al [38] replaced the cathode GDL with metal foams and achieved higher gas permeability and lower contact resistance, which enabled the current density enhancement by about 20% at 0.6 V. Different flow field designs were investigated by Bandlamudi et al. [39] and the results reveals that the increment of Pt crystal growth and decrease of active reaction surface lead to higher ohmic resistance.

Among all the components of PEMFC, bipolar plates are of great significance to the flow field inside the gas channels, GDLs and CLs. They play vital roles in not only the gas supply but also the collection of generated current [40]. These plates also provide mechanical strength of the cell and participate in the management of heat and water produced [41]. The value of channel divided by rib width is one of the most important parameters of bipolar plates. Wang et al. [42] numerically analyzed this parameter's effect for five values: 0.43, 0.66, 1.06, 1.5, 2.33 and reported that higher ratio brings better performance due to easier gas transport. Hyun et al. [43] studied the effect of under-rib convection in PEM fuel cell and reported that better under-rib gas transport and cell performance could be enhanced with larger path-length variation between adjoining gas flow channels. Shimalee et al. [44] numerically studied the

effect of different rib and channel dimensions and found that narrower channel with a wider rib leads to better cell performance. Kerkoub et al. [45] investigated different geometry designs of bipolar plates and reported that, the channel to rib width ratios (CRWR) would significantly affect cell behavior at low voltage while slight change on cell behavior was observed at a high voltage.

The above-mentioned numerical studies on the CRWR have all been done for low temperature PEMFC (LT-PEMFC). Besides, heat transfer and the thermal effects are not considered. The effects of CRWR on electrochemical behavior of HT-PEMFC remains unknown. It should be mentioned that it is necessary to conduct a comprehensive study to illuminate the rib size effect as the conclusions from the LT- PEMFC cannot be directly applied to HT-PEMFC due to the significantly different transport mechanisms. In LT-PEMFCs, the liquid-gas two-phase flow inside the cell must be carefully considered since the operating temperature is below 100 ºC. In HT-PEMFCs, water molecules exist in the form of the water vapor. The transport characteristics, temperature distribution and electrochemical behaviors of HT-PEMFC and LT-PEMFC can greatly differ.

To fill in the above-mentioned research gap, a three-dimensional, non-isothermal HT-PEMFC model was developed to elucidate how the value of CRWR would affect the electrochemical behavior and temperature field of HT-PEMFC, which is the main contribution of this study. In addition, temperature-dependent physical properties are used in the present study, instead of constant properties as used in the previous studies. The numerical model is validated, followed by parametric simulations.

2. Modelling

2.1 Description and assumptions of model

Fig.1 shows the working principle of HT-PEMFC. The anode gas channel gets supplied with hydrogen (H_2) fuel while cathode gas channel gets supplied with air or pure oxygen (O_2), respectively. H_2 molecules diffuse from the channel into the GDL and are electrochemically oxidized in CL to produce protons and electrons. The protons are transferred through the polybenzimidazole (PBI) electrolyte membrane to the cathode by the process of "Grotthus mechanism" [46]. The protons, electrons and the O_2 molecules electrochemically combine to form H_2O vapor molecules at cathode side.

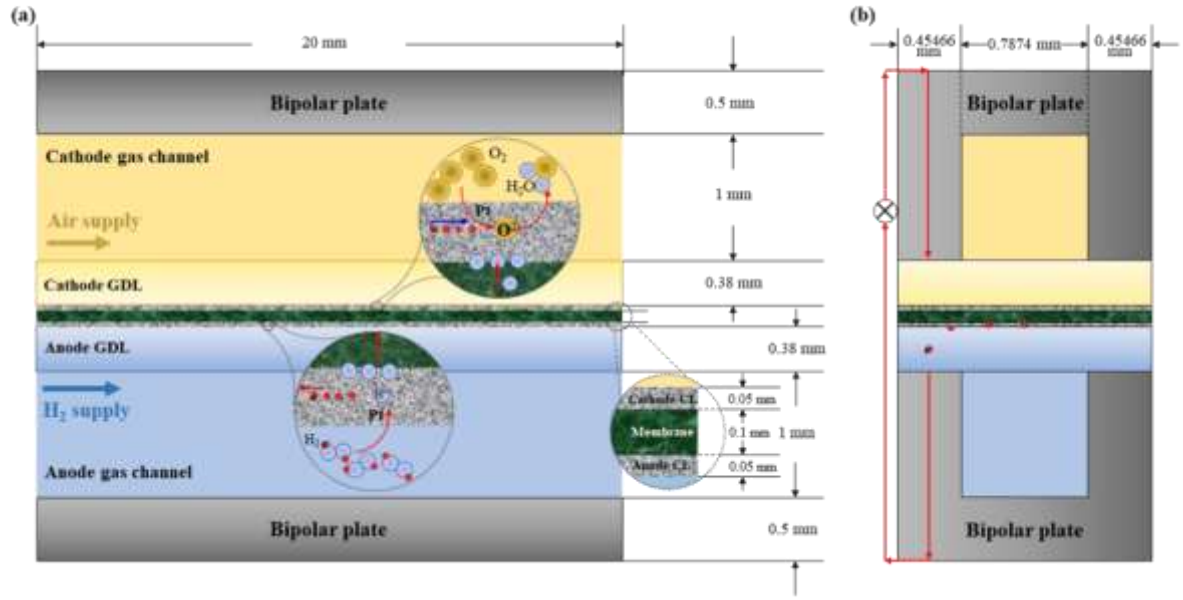

Fig.1. Schematic and computational geometry of high temperature proton exchange membrane fuel cell (a) y-z perpendicular plane (b) x-z vertical plane

The geometric parameters of HT-PEMFC are listed in Table 1. Following assumptions are adopted in this three-dimensional non-isothermal model: (1) Gas mixtures obey ideal gas law; (2) The gas flow is fully developed laminar flow; (3) Proton exchange membrane (PEM) is impermeable to all gases; (4) Porous media including GDLs and CLs are isotropic and homogeneous; (5) HT-PEMFC works in steady state. The other cell physical/chemical

properties and operating parameters are shown in Table 2. For the purpose of model validation, most of the physical properties and working conditions are consistent with the values measured by experiment [47]. For example, the channel width and rib width are 0.7874mm and 0.9093mm, respectively, giving a channel to rib ratio of about 0.87. However, different from ref. [47], temperature-dependent physical parameters are used, including the diffusion coefficient, ionic conductivity of electrolyte, dynamic viscosity of gases, heat capacity and heat conductivity.

Parameter	Value
Channel length	20 [mm]
Channel height	1 [mm]
Channel width	0.7874 [mm]
Rib height	1 [mm]
Rib width	0.9093 [mm]
GDL thickness	0.38 [mm]
CL thickness	0.03 [mm]
Membrane thickness	0.06 [mm]
Collector thickness	0.5 [mm]

Table 1 Geometric parameters

Parameters	Value
Humidified temperature, T_H	28 [°C]
Working temperature, T_w	180 [°C]
GDL porosity, ε_{GDL}	0.4
GDL permeability, K_{GDL}	1.18e-12 [m^2]
CL porosity, ε_{CL}	0.4
Cl permeability, K_{CL}	K_{GDL} /5 [m^2]
Anode stoichiometry number, λ_a	1.2
Cathode stoichiometry number, λ_c	2.0
Molar fraction of H_2, w_{H2}	0.963
Molar fraction of H_2O, w_{H2O}	0.037
Molar fraction of O_2, w_{O2}	0.202
Molar fraction of N_2, w_{N2}	1- w_{O2} -w_{H2O}
Molar mass of H_2, M_{H2}	2 [g/mol]
Molar mass of N_2, M_{N2}	28 [g/mol]
Molar mass of H_2O, M_{H2O}	18 [g/mol]
Molar mass of O_2, M_{O2}	32 [g/mol]

Anode exchange current density, $i_{0,a}$	1e5 [A/m^2]
Cathode exchange current density, $i_{0,c}$	1 [A/m^2]
Anode charge transfer coefficient, α_a	1
Cathode charge transfer coefficient, α_c	1
Electrolyte conductivity at 180^{o}C, σ_e	9.825 [S/m]
Electrode conductivity, σ_s	222 [S/m]
Bipolar plate conductivity, σ_b	20,000 [S/m]
Reference pressure, P_r	1 [atm]

Table 2 Physical/chemical properties and operating conditions [47]

2.2 Governing equations

2.2.1 Flow field

The gas flows are laminar in channels and Navier-Stokes equation is adopted for modelling the momentum transfer:

$$\rho(\frac{\partial \vec{v}}{\partial t} + \vec{v} \bullet \nabla \vec{v}) = \nabla \left\{ -P\vec{I} + \mu[\nabla \vec{v} + (\nabla \vec{v})^T] \right\} \quad (1)$$

where x_i is the molar fraction of specific specie, R is universal gas constant, T is working temperature. The inlet gas's velocity is calculated by:

$$U_{in\_cathode} = \lambda_c \frac{I}{4F} x_{O_2} RT / (P \bullet A_{channel} \bullet n_{channel}) \quad (2)$$

$$U_{in\_anode} = \lambda_a \frac{I}{2F} x_{H_2} RT / (P \bullet A_{channel} \bullet n_{channel}) \quad (3)$$

where $U_{\text{in\_cathode}}$ is the average velocity, A_{channel} is area of gas channel perpendicular to the direction of fluid flow and n_{channel} represents the number of channels which is set as 1 in this model. The dynamic viscosities of each species are listed in Table 4 with temperature effect considered. Thus, gas mixture's dynamic viscosity can be calculated by [48]:

$$\mu_{a,c} = \sum_{i=1}^{n} \frac{y_i \mu_i}{\sum_{j=1}^{n} (y_j \sqrt{\frac{M_j}{M_i}})} \quad (4)$$

2.2.2 Mass transport

The mass transport in cathode is governed by:

$$\nabla\left\{-\rho w_i\sum_{j=1}^{N}D_{ij}[\frac{M}{M_j}\left(\nabla w_j+w_j\frac{\nabla M}{M}\right)+\left(x_j-w_j\right)\frac{\nabla P}{P}]+w_i\rho\vec{v}\right\}=R_i \tag{5}$$

where D_{ij} is the binary diffusion coefficient and be correlated with:

$$D_{ij}=D_{ij\_0}(\frac{T}{T_0})^{1.5} \tag{6}$$

At cathode, the mole fraction of oxygen is solved with nitrogen and water by:

$$w_{N_2}=1-w_{O_2}-w_{H_2O} \tag{7}$$

The multicomponent density is governed by:

$$\rho=\mathrm{p}(\mathrm{RT}\sum_i\frac{Y_i}{M_i})^{-1} \tag{8}$$

where p is the gas pressure, Y_i is mass fraction of species i and M_i is molar mass of species i.

2.2.3 Heat transfer

The heat release caused by electrochemical reaction (Q_{react}) can be calculated by:

$$Q_{\mathrm{react}}=(-T\Delta S)\cdot\frac{I}{nF} \tag{9}$$

where ΔS is the entropy change of the reaction, I is the current density. However, since the half reactions of hydrogen oxidation and oxygen reduction take place at different positions separately, the reaction heats for the two half reactions should be calculated respectively for the two electrodes.

Anode: $$H_2\rightarrow 2H^++2\mathrm{e}^- \tag{10}$$

Cathode: $$\frac{1}{2}O_2+2H^++2\mathrm{e}^-\rightarrow H_2O \tag{11}$$

The entropy changes of hydrogen oxidation $\triangle S_a$ and $\triangle S_c$ can be calculated respectively by:

$$\Delta S_a=2S^\circ[H^+(g)]+2S^\circ[e^-(g)]-S^\circ[H_2(g)] \tag{12}$$

$$\Delta S_{\mathrm{c}}=S^\circ[H_2O(g)]-2S^\circ[e^-(g)]-2S^\circ[2H^+(g)]-\frac{1}{2}S^\circ[O_2(g)] \tag{13}$$

where $S^\circ[i]$ is the absolute entropy of species i taken from NIST-JANAF Table [49] and is listed in Table 3. The entropy changes of hydrogen oxidation and oxygen reduction at any other

temperatures can then be calculated by a quartic polynomial fitting curve. The other thermal properties are listed in Table 4.

Beside the heat release caused by the entropy change, another heat release produced by ohmic loss is given by:

$$Q_{\mathrm{oh}} = (U_0 - V_{cell}) \cdot I \cdot A_{\mathrm{react}} \tag{14}$$

where U_0 is the equilibrium voltage and V_{cell} is the output voltage. It is noted that the local U_0 is calculated using the local temperature and local gas composition, as both temperature and gas composition vary in the 3D structure. I represents the local current density. Gas diffusion in the porous layer including the catalyst layer is solved to determine the gas composition distribution in the 3D porous structure. Inside CL, the local heat generation by ohmic loss can be calculated by:

$$Q_{\mathrm{oh}} = \left\|\nabla \varphi_{ele}\right\|^2 \sigma_{ele}^{eff} + \left\|\nabla \varphi_{pro}\right\|^2 \sigma_{pro}^{eff} \tag{15}$$

where φ_{ele} and φ_{pro} represent the local potentials of electrode and electrolyte materials in the catalyst layer, σ_{ele} and σ_{pro} represent the conductivity of electron and proton. σ^{eff} represents the effective conductivity with due consideration of porosity. Thus, the total heat release Q_{total} can be calculated by:

$$Q_{\mathrm{total}} = Q_{\mathrm{react}} + Q_{\mathrm{oh}} + Q_{\mathrm{act}} \tag{16}$$

where Q_{act} is the heat generation caused by activation loss. Q_{act} at both anode and cathode can be calculated by:

$$\begin{aligned} Q_{\mathrm{act\_a}} &= j_a \left|\eta_{act}\right| \\ Q_{\mathrm{act\_c}} &= j_c \left|\eta_{act}\right| \end{aligned} \tag{17}$$

The heat transfer is governed by energy equation:

$$\nabla \cdot (\rho C_{\mathrm{p}} \vec{v} T) = \nabla \cdot (\lambda \nabla T) + S_T \tag{18}$$

where λ is the gas mixture's thermal conductivity, S_T represents the heat source due to electrochemical reaction and various irreversible losses, C_p is the gas mixture's heat capacity and they are calculated by each specie's mass fraction and its properties:

$$C_{\mathrm{p}} = \sum_i Y_i (C_{\mathrm{p}})_i \tag{19}$$

$$\lambda = \sum_i Y_i \lambda_i \tag{20}$$

2.2.4 Electronic field

The current densities at two catalyst layers are governed by the equation (9) and (10):

$$i_a = i_{0,a} \left(\frac{C_{H_2}}{C_{H_2,ref}}\right)^{0.5} \left(e^{\frac{n\alpha_a F}{RT}\eta_a} - e^{\frac{-n(1-\alpha_a)F}{RT}\eta_a} \right) \tag{21}$$

$$i_c = i_{0,c} \left(\frac{C_{O_2}}{C_{O_2,ref}}\right)^{1} \left(-e^{\frac{n(1-\alpha_c)F}{RT}\eta_c} + e^{\frac{-n\alpha_c F}{RT}\eta_c} \right) \tag{22}$$

where a is the ratio of reaction surface, $i_{0,\,a/c}$ is the anode/cathode's exchange current density, c_{H2} is the concentration of H_2, $c_{H2,\,ref}$ is the reference concentration of H_2, F is Faraday's constant, and $\alpha_{a/c}$ is the transfer coefficients of the anode/cathode. Then the current can be calculated by:

$$i = \frac{1}{A_{\mathrm{act}}} \int_{A_{\mathrm{act}}} i_{loc} dA \tag{23}$$

where A_{act} is active area of the reaction. Since the temperature gradient exists in the fuel cell, the membrane conductivity gets correlated by the following equation:

$$\sigma_{\mathrm{mem}} = \sigma_0 \exp\left[\frac{E_a}{R}(-1/T + 1/453.15)\right] \tag{24}$$

where σ_0 is the membrane conductivity at 180 °C, E_a is the activation energy calculated by the linear fitting curve [50]:

$$E_a = -619.6DL + 21750 \tag{25}$$

where DL is PBI membrane's doping level of phosphoric acid and is set as 5 based on reference

[12]. Inside catalyst layer, the transport of the ions and electrons can be described by ohm's law. As the catalyst layer is porous, the effective conductivity should be modified with due consideration of the porosity effect, as shown as the Bruggeman equation:

$$\sigma_{l,\mathrm{CL}} = \varepsilon_l^{1.5}\sigma_l \tag{26}$$

The output voltage is governed by:

$$V = E_{thermo} - \eta_{act} - \eta_{ohmic} - \eta_{conc} \tag{27}$$

where E_{thermo} is the ideal voltage, η_{act}, η_{ohmic}, η_{conc} represent the activation loss, ohmic loss and concentration loss, respectively. The local ideal voltage is calculated using the local temperature and local gas composition, which vary in 3D in the HT-PEMFC. For activation loss η_{act}, it can be calculated by following equation:

$$\eta^a_{\mathrm{local}} = \phi^a_{\mathrm{local},s} - \phi^a_{\mathrm{local},l} - E^a_{eq} \tag{28}$$

$$\eta^c_{\mathrm{local}} = \phi^c_{\mathrm{local},s} - \phi^c_{\mathrm{local},l} - E^c_{eq} \tag{29}$$

where ϕ represents the local electric potential and E_{eq} represents the local equilibrium electric potential. The values at two electrodes are governed by equation:

$$E^a_{eq} = 0; \quad E^c_{eq} = E_{Nernst} \tag{30}$$

For ohmic loss η_{ohmic}, it can be calculated with the ohm's law using the local current density, electron transfer distance and effective electron conductivity. Gas diffusion in the porous electrodes is solved to determine the local gas composition in the 3D porous electrodes, which is used for the calculation of the activation loss in the Butler Volmer equation.

Temperature [K]	H_2 [J·K^{-1}·mol^{-1}]	O_2 [J·K^{-1}·mol^{-1}]	H^+ [J·K^{-1}·mol^{-1}]	e^- [J·K^{-1}·mol^{-1}]	H_2O [J·K^{-1}·mol^{-1}]
298.15	130.68	205.157	108.946	20.979	188.834
300	130.858	205.329	109.075	21.107	189.042
350	135.315	209.88	112.279	24.311	/
400	139.216	213.871	115.055	27.087	198.788
450	142.656	217.445	117.503	29.535	/
500	145.737	220.693	119.693	31.725	206.634

Table 3 Absolute entropy of each specie

Parameters	Value
Dynamic viscosity of H_2	(27.758+2.12E-1*T-3.28E-5*T*T) *1e-7 [Pa·s]
Dynamic viscosity of N_2	(42.606+4.75E-1*T-9.88E-5*T*T) *1e-7 [Pa·s]
Dynamic viscosity of O_2	(44.224+5.62E-1*T-1.13E-5*T*T) *1e-7 [Pa·s]
Dynamic viscosity of H_2O	(-36.826+4.29E-1*T-1.62E-5*T*T) *1e-7 [Pa·s]
Heat capacities of H_2	25.40+2.0178E-2*T-3.8549E-5*T^2+3.1880E-8*T^3-8.7585E-12*T^4 [J/mol/K]
Heat capacities of N_2	29.34-3.5395E-3*T+1.0076E-5*T^2-4.3116E-9*T^3+2.5935E-13*T^4 [J/mol/K]
Heat capacities of O_2	29.53-8.8999E-3*T+3.8083E-5*T^2-3.2629E-8*T^3+8.8607E-12*T^4 [J/mol/K]
Heat capacities of H_2 O	33.93-8.4186E-3*T+2.9906E-5*T^2-1.7825E-8*T^3+3.6934E-12*T^4 [J/mol/K]
Thermal conductivities of H_2	0.03591+4.5918E-4*T-6.4933E-8*T^2 [W/m/K]
Thermal conductivities of N_2	0.00309+7.5930E-5*T-1.1014E-8*T^2 [W/m/K]
Thermal conductivities of O_2	0.00121+8.6157E-5*T-1.3346E-8*T^2 [W/m/K]
Thermal conductivities of H_2O	0.00053+4.7093E-5*T+4.9551E-8*T^2 [W/m/K]

Table 4 Thermal properties [51]

2.3 Boundary conditions

The HT-PEMFC works under the mode of open-end for both anode and cathode. The proton exchange membrane is set to be impermeable to all reactant gases. Back pressures of both anode and cathode outlets are atmospheric pressure. Molar fractions of species at inlet are calculated based on the humidified air and the corresponding temperature is 28 °C.

The surface of cathodic current collector is connected to the electrical ground with $\phi_s = 0$ while the fixed potential with $\phi_s = V_{\text{cell}}$ is set at the surface of anode current collector. As the present model considers a repeating unit cell from a large fuel cell stack, it is reasonable to

assume that each unit cell behaves identically. Thus, there is no heat transfer between each unit cell. In this work, the surface of the bipolar plate is adiabatic. The generated heat is taken out from the fuel cell by gas flow. The other walls of the entire domain are set to be insulated both for electricity and heat. The internal surface is assumed to be no-slip.

3. Results and discussions

3.1 Validation of model

3.1.1 Grid independence analysis

Fig.2 shows the result of grid independence analysis. The results show that the computed current density at 0.55 V gradually approaches a constant value when the number of meshing elements is higher than 20,000. As expected, the solution time increases almost linearly with increasing number of meshing elements. The grid consisting of 21190 elements required 75-minutes solution time while a grid of 47736 elements would cost 163 minutes with a slight improvement in the accuracy of the result. Taking both the result accuracy and efficiency into consideration, the meshing number of 21190 elements is adopted in the subsequent study.

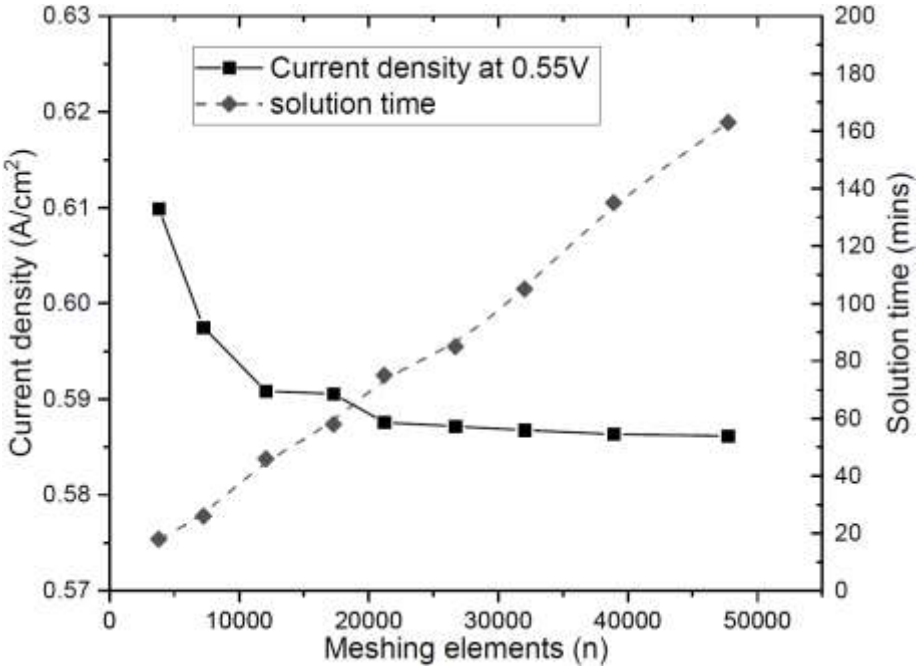

Fig.2. Grid independence analysis

3.1.2 Model validation

Preliminary simulation is conducted for comparison with experimental data from the literature for model validation. In the experiment, the fuel cell works under the operating temperature of 180 °C at the atmospheric pressure. Stoichiometry number are 1.2 and 2 for anode and cathode respectively with the reference current density to be 1.0 A/cm^2. The doping level of phosphoric acid in the PBI membrane is 5. The value of CRWR adopted for validation is 0.87 which can be calculated by the geometric parameters listed in Table 1. The dimensions and operating parameters in reference [47] are adopted in the simulation for comparison. As shown in Fig.3, the simulation results agree very well with experimental data from Ref. [47], thus validate the developed model.

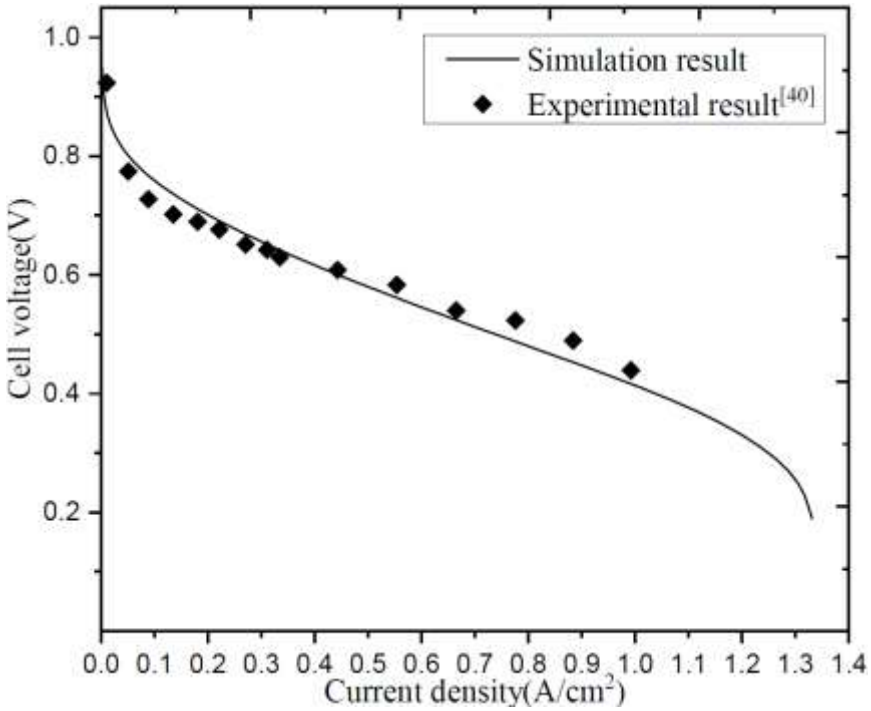

Fig.3. Grid independence analysis

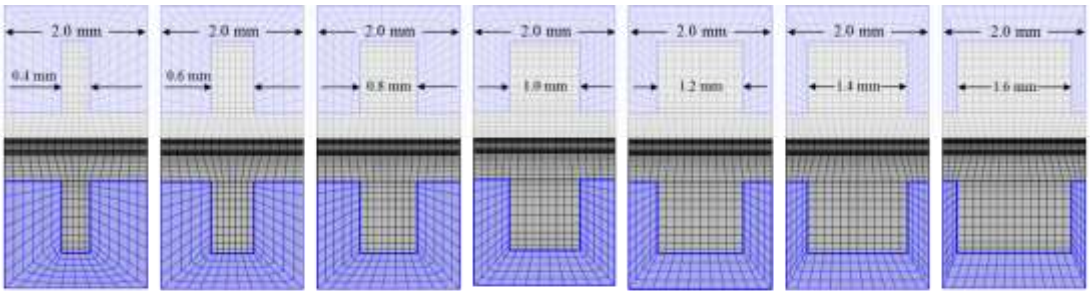

Channel[mm]	0.4	0.6	0.8	1	1.2	1.4	1.6
Rib[mm]	1.6	1.4	1.2	1	0.8	0.6	0.4
Ratio	0.25	0.43	0.67	1	1.5	2.33	4

Fig.4. Rib design with different values of CRWR

After validating this model, various values of CRWR are adopted for further research. Fig.4 shows the details of each design. The ratio is defined as the channel width divided by the rib width. In this case, 7 ratios including 0.25, 0.43, 0.67, 1, 1.5, 2.33 and 4 are selected to investigate its effect on species transport, temperature growth/distribution and cell performance. For comparison, the same flowrate is adopted for different designs.

3.2 Reactants transport and distribution

Fig.5 shows the distributions of reactants at different positions with different values of

CRWR at an operating voltage of 0.5 V. The oxygen concentration at the gas channel is always higher than that at GDL and CL in Fig.5 (a). Besides, the value of oxygen concentration gradually decreases from the inlet to the outlet because of the cathodic oxygen reduction reaction (ORR). The oxygen distribution at the GDL and CL with the ratio of 0.25 is extremely nonuniform. Fewer oxygen molecules can be diffused to the porous cathode under the rib. With increasing ratio, oxygen distribution becomes more uniform, due to shorter distance for gas diffusion under the rib.

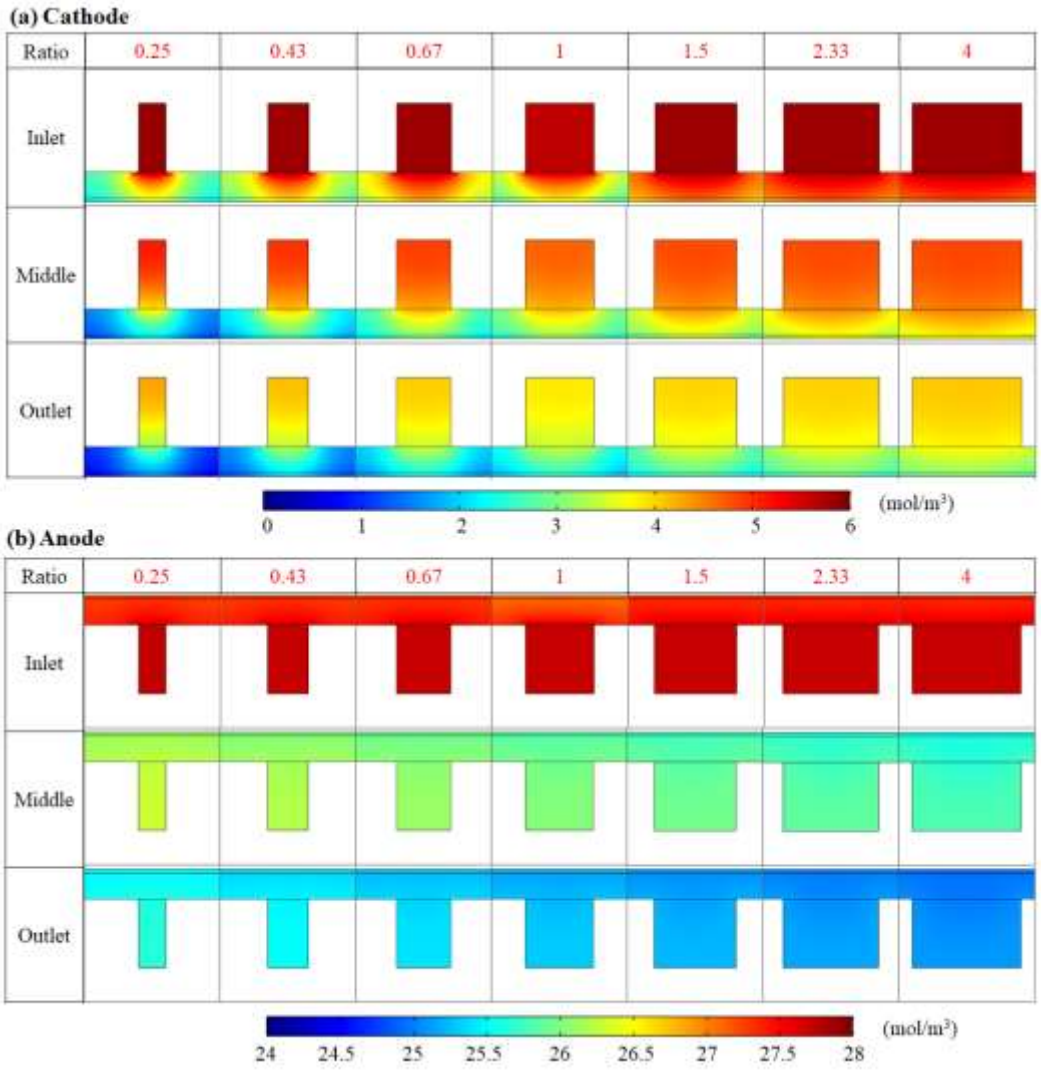

Fig.5. Distribution of reactants at different positions. (a) Oxygen distribution at cathode; (b) Hydrogen distribution at anode

For comparison, the hydrogen distribution is much more uniform than that of the oxygen with the same ratio. This is due to the smaller molecular size and molar mass of hydrogen molecule compared with the oxygen molecule. According to the Matheson gas data book [52], the kinetic diameters of hydrogen molecule and oxygen molecule are 2.89 Å and 3.46 Å, respectively. Similarly, the hydrogen concentration decreases along the flow direction because of fuel oxidation reaction at anode. To conclude, increasing the value of CRWR significantly improve the uniformity of oxygen distribution in the porous cathode while its influence on the anode fuel distribution is insignificant as the fast H_2 diffusion ensures uniform fuel distribution.

Fig.6 (a) shows the current densities distribution with oxygen distribution added at various ratios. When a ratio 0.25 is adopted, the current density at two sides are significantly lower than that at the middle area because of the low oxygen concentration here. As the ratio increases from 0.25 to 0.67, an evener current density distribution can be acquired due to the better diffusion of oxygen distribution. However, a relatively low current density area emerges at the middle area with a higher ratio. This can be attributed by the increasing electron resistance. Two designs with ratio to be 1 and 4 are selected for analysis in Fig.6 (b).

When ratio to be 1 is adopted, the straight-line distance for the electron transferring from middle area to the bipolar plates is 0.628 mm shown in Fig.6 (c). After raising the ratio to 4, the straight-line distance grows to 0.886 mm in Fig.6 (d). Moreover, the electron trajectory would be more complex in fact since the GDL and CL are both porous media and the electron cannot be transferred through the pores as shown in Fig.6 (e & f). In other words, the distance for the electron transfer would be longer and the electron resistance will increase further. Therefore, the low current density occurs at the middle area when adopting a higher ratio even

the higher ratio brings a better reactants distribution (Fig.6 (b)).

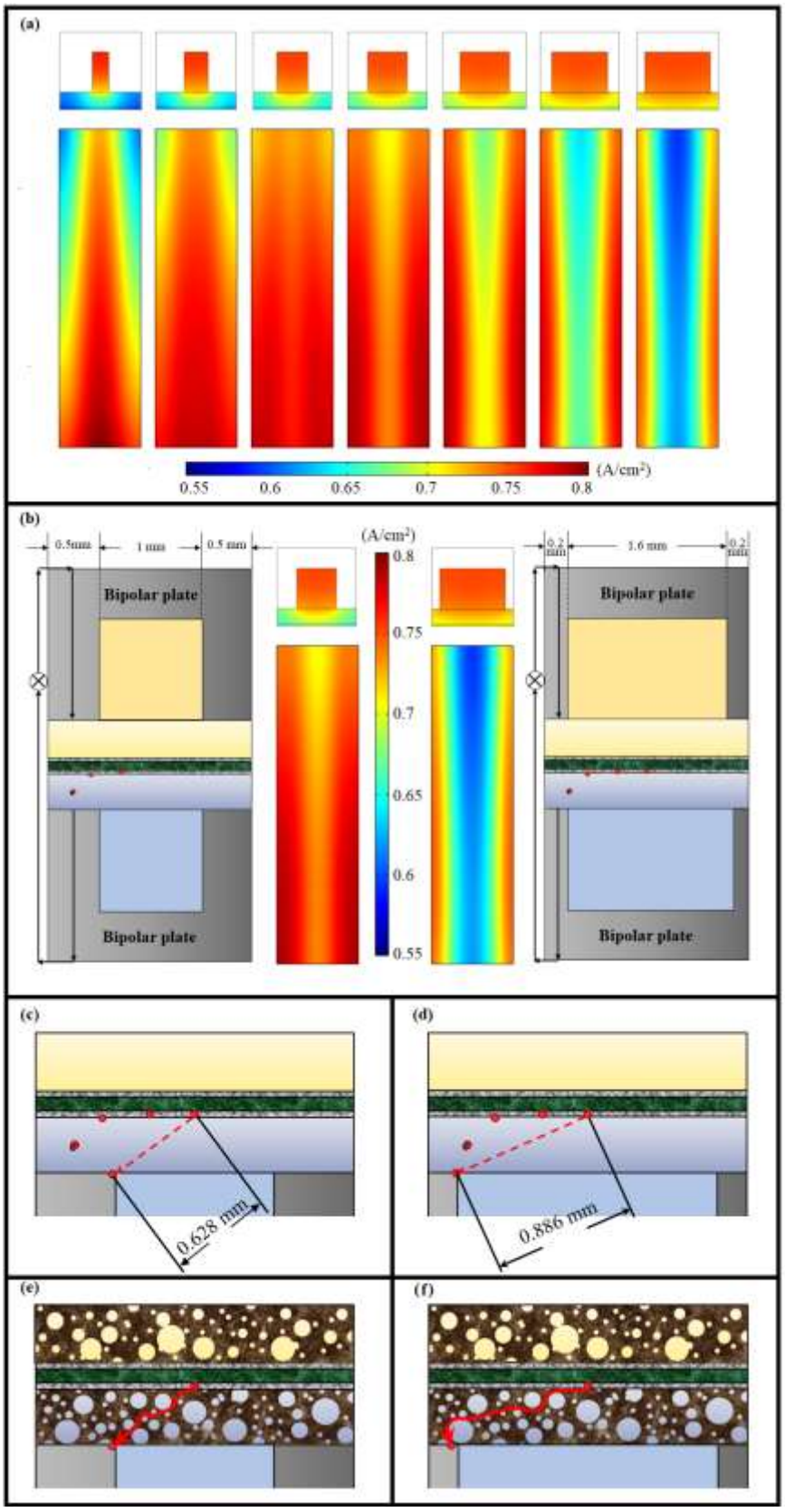

Fig.6. (a) Current densities distribution with different CRWRs; (b) Fabrications of two kinds

of fuel cells; (c) Electron transfer with CRWR to be 1 in the model; (d) Electron transfer with CRWR to be 4 in the model; (e) Electron trajectory in porous media in the first design; (f) Electron trajectory in porous media in the second design.

3.3 Temperature distribution and gradient

Fig.7 shows the temperature distributions on all three x-z, y-z, x-y planes at the y = 0.01m, x = 1mm and z = 2.03mm respectively (middle along the flow direction, middle along cell width and middle along cell height) at different values of CRWR. The cell is operated at a voltage of 0.5V. The temperatures of both anode and cathode gas inlets are 150 °C.

As shown in Fig.7 (a), MEA's temperature is always higher than the temperature of bipolar plates and gas channels since most of heat comes from the MEA due to entropy change and overpotential losses. The cathode temperature is always higher than that of anode because of the larger activation loss of ORR. Similar result of temperature distribution was reported by Jiao et al. [50]. In their work, the temperature was fixed as a constant on the surrounding walls, which leads to an unchanged temperature of bipolar plate. However, the bipolar plate has a high thermal conductivity and the heat generated from the MEA can be easily conducted to the plate, causing the temperature of the bipolar plate to increase.

An interesting phenomenon appears that there is a circular area representing low temperature in the cathode channel. This is because the high thermal conductivity of the bipolar plate causes its temperature to go up easily. For comparison, the cathode gas temperature is relatively low since the high gas velocity in the cathode results in a short time for heating cathode gas. Compared with cathode gas flow, the velocity of anode gas flow is about 4 to 5 times smaller, which will result in a longer heating time for H_2 gas. Thus, the low-temperature

circular area doesn't appear in anode channel. Comparing the temperature distributions with different ratios in Fig.7 (b & c), the temperature normally increases along the gas channel.

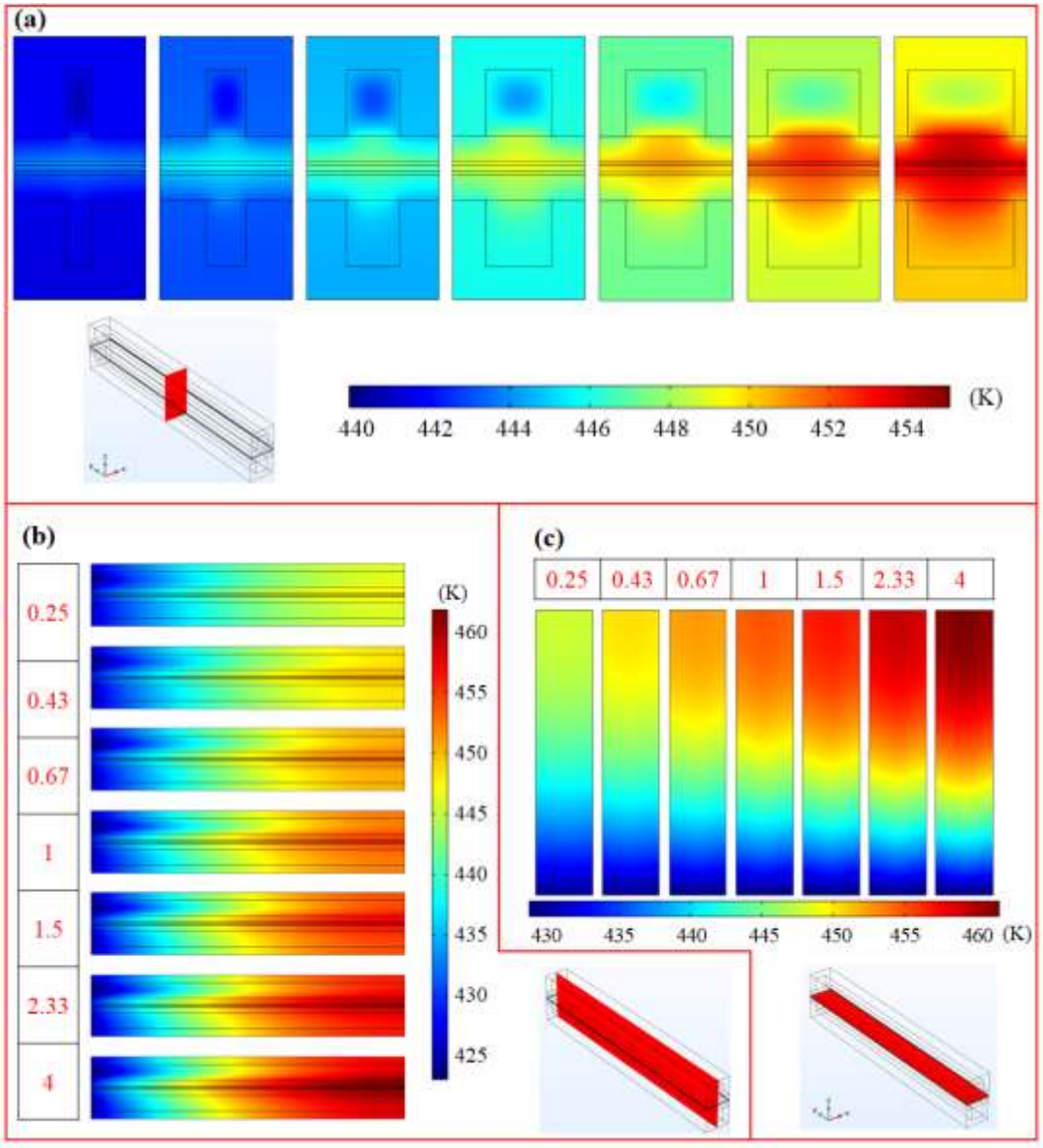

Fig.7. Temperature distribution at different planes. (a) Longitudinal section; (b)Vertical section; (c) Horizontal section

Since the temperature in the HT-PEMFC varies significantly, it is important to investigate the temperature gradient in HT-PEMFC, which is closely associated with the thermal stress in the HT-PEMFC. Fig.8 shows the computed temperature change and gradient at cathode, membrane and anode. The initial temperatures of both anode and cathode inlets are 423.15 K

in Fig.8 (a & c) while the membrane temperature begins from about 429 K in Fig.8 (b) due to the thermal insulation condition specified at the inlet of the MEA. It is found that the temperature increment along the channel always increases with increasing ratio of channel to rib width. The maximum cell temperature growth of 38.51 K occurs at membrane with the CRWR value of 4. The other two maximum cell temperature growths at cathode and anode are 35.63 K and 35.96 K, respectively.

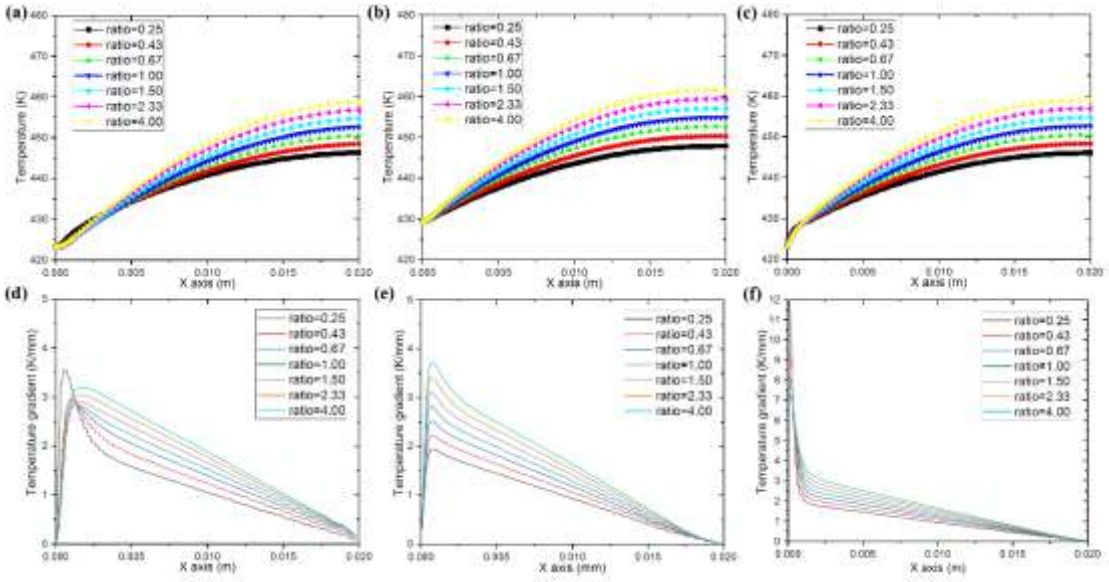

Fig.8. Temperature growth and gradient along the length at different components with different CRWRs. (a) Temperature growth at cathode; (b) Temperature growth at membrane; (c) Temperature growth at anode; (d) Temperature gradient at cathode; (e) Temperature gradient at membrane; (f) Temperature gradient at anode.

As shown in Fig.8 (d & e), the temperature gradients first rapidly reach to a peak value and then go down steadily. At cathode, the x values of the peak points increase with ratio ranging from 0.25 to 1 and decrease when the ratio keeps rising. At membrane, both the peak values and its x positions increase when a higher ratio is adopted. However, the temperature gradient at anode has a continuous decline along the flow direction. Such a high temperature

gradient at gas channels and membrane near the inlet may cause a considerable thermal stress and thus degradation of the HT-PEMFC life [53]. So, it's highly recommended to take some protective measures near the gas inlet when specific design is adopted.

3.4 Cell performance

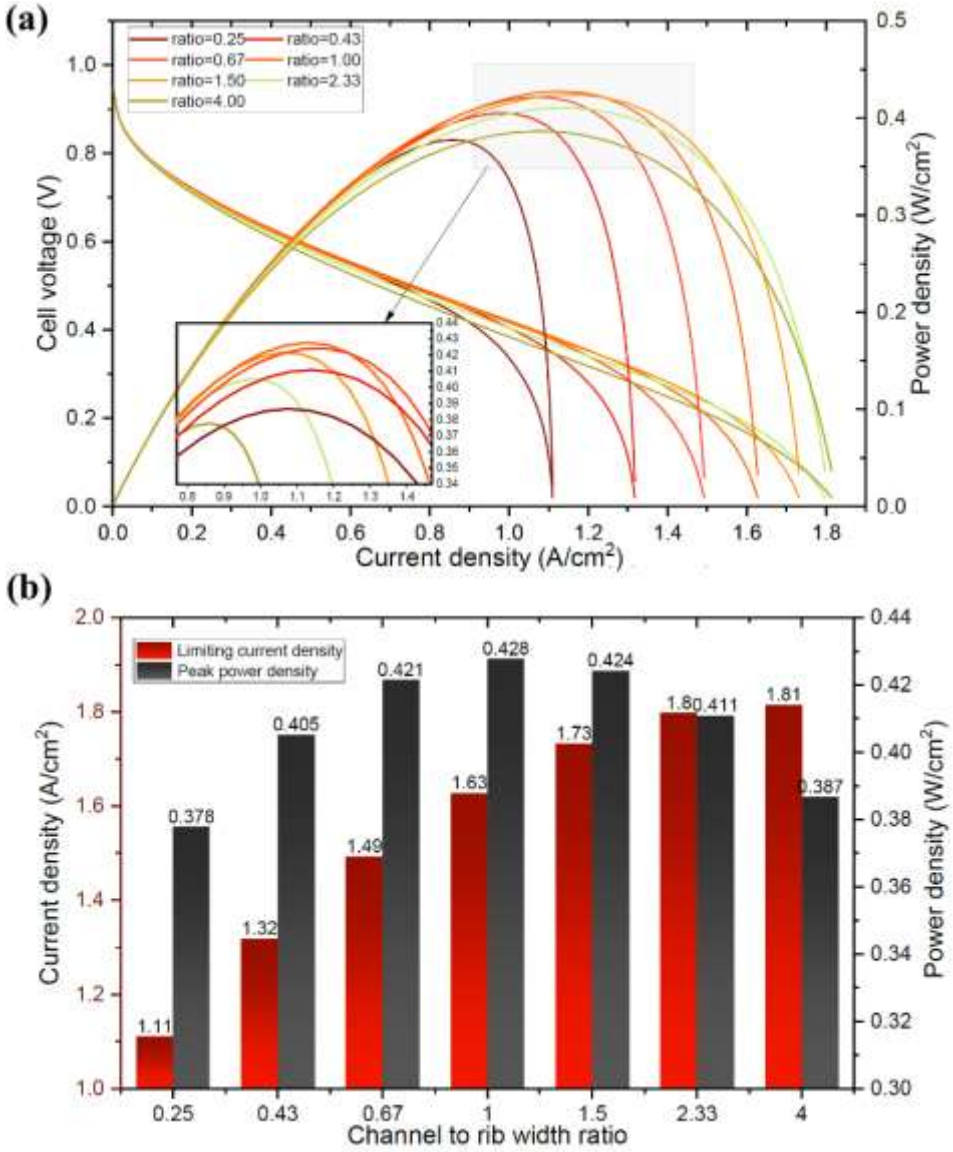

Fig.9. Cell performance with different CRWRs. (a) Polarization curve of cell voltages and power densities; (b) Limiting current densities and peak power densities.

Fig.9 (a) shows the polarization curves of both cell voltages and power densities. On the whole, a better cell performance can always be expected when the ratio increases from 0.25 to

1, not only the higher power density but also bigger range of current density. The voltage polarization curves with ratio to be 1 and 1.5 are almost same, but the latter one would bring a higher limiting current density, indicating the improved gas transport in the cell. When the ratio rises further, a drop of cell performance would appear. The ohmic resistance is a little bit higher with ratio to be 4 than that with ratio to be 1.

For better illustration, the peak value of power density and limiting current densities with various designs are extracted and shown in Fig.9 (b). The maximum value of power density 0.428 W/cm^2 can be obtained with ratio to be 1. The limiting current density has a positive correlation with the value of CRWR while the growth rate is getting smaller. The cell design with ratio to be 4 has the largest limiting current density of 1.81 A/cm^2.

4. Conclusion

In this work, a three-dimensional, non-isothermal HT-PEMFC model was developed. Entropy changes of half-reactions were considered. The objective of this work is to evaluate how the value of CRWR influence the gas distribution, current density, temperature and cell performance of HT-PEMFC.

Due to the fast hydrogen diffusion, the fuel distribution in the porous anode is rather uniform. For comparison, the slow diffusion of O_2 molecules in the porous layer causes the O_2 distribution in the cathode to be highly dependent on the CRWR. At a low ratio value, the distribution of O_2 in the porous cathode is highly non-uniform and the O_2 concentration under the rib is rather low. The O_2 distribution becomes more uniform with increasing ratio of channel to rib width. However, a thinner rib results in longer distance for electron conduction from the porous GDL to the bipolar plate, leading to high ohmic loss. Thus, high current density is

observed under the channel with a small ratio value while high current density is found under the rib with a high ratio value. As a result, an optimal ratio of about 1 is observed, which results in a peak power density of 0.428 W/cm^2.

In addition to the electrical power output, the ratio of channel to rib width also has a significant effect on the fluid flow and temperature distribution inside the HT-PEMFC. MEA's temperature is always higher than the temperature of bipolar plates and gas channels since most of heat comes from the MEA due to entropy change and overpotential losses. Due to the larger activation loss of ORR, the cathode temperature is always higher than that of anode. It is found that the temperature increment along the channel always increases with increasing ratio of channel to rib width. The maximum cell temperature growth of 38.51 K occurs at membrane with CRWR value of 4. Near the inlet, there is always a peak temperature gradient which may cause a considerable thermal stress and thus influence the long-term stability of the cell.

In the subsequent studies, efforts will be made to develop new stack configurations with more uniform gas distribution, short electron conduction path and low temperature gradient.

Acknowledgement

M. Ni thanks the funding support (Project Number: PolyU 152214/17E and PolyU 152064/18E) from Research Grant Council, University Grants Committee, Hong Kong SAR.

Reference

[1] Rosli R, Sulong A, Daud W, Zulkifley M, Husaini T, Rosli M, et al. A review of high-temperature proton exchange membrane fuel cell (HT-PEMFC) system. International Journal of Hydrogen Energy. 2017;42:9293-314.

[2] Zhou S, Dhupia JS. Online adaptive water management fault diagnosis of PEMFC based on orthogonal linear discriminant analysis and relevance vector machine. International Journal of Hydrogen Energy. 2020;45:7005-14.

[3] Moçotéguy P, Ludwig B, Beretta D, Pedersen T. Study of the impact of water management on the performance

of PEMFC commercial stacks by impedance spectroscopy. International Journal of Hydrogen Energy. 2020;45:16724-37.
[4] Li C, Si D, Liu Y, Zhang J, Liu Y. Water management characteristics of electrospun micro-porous layer in PEMFC under normal temperature and cold start conditions. International Journal of Hydrogen Energy. 2021; 46(19)11150-11159.
[5] Zamel N, Li X. Transient analysis of carbon monoxide poisoning and oxygen bleeding in a PEM fuel cell anode catalyst layer. International Journal of Hydrogen Energy. 2008;33:1335-44.
[6] Li Q, He R, Gao J-A, Jensen JO, Bjerrum NJ. The CO poisoning effect in PEMFCs operational at temperatures up to 200 C. Journal of the Electrochemical Society. 2003;150:A1599.
[7] Brouzgou A, Seretis A, Song S, Shen PK, Tsiakaras P. CO tolerance and durability study of PtMe (Me= Ir or Pd) electrocatalysts for H2-PEMFC application. International Journal of Hydrogen Energy. 2020. in press.
[8] Zhang J, Xiang Y, Lu S, Jiang SP. High temperature polymer electrolyte membrane fuel cells for integrated fuel cell–methanol reformer power systems: a critical review. Advanced Sustainable Systems. 2018;2:1700184.
[9] Andreasen SJ, Vang JR, Kær SK. High temperature PEM fuel cell performance characterisation with CO and CO2 using electrochemical impedance spectroscopy. International journal of hydrogen energy. 2011;36:9815-30.
[10] Asensio JA, Sánchez EM, Gómez-Romero P. Proton-conducting membranes based on benzimidazole polymers for high-temperature PEM fuel cells. A chemical quest. Chemical Society Reviews. 2010;39:3210-39.
[11] Lakshminarayana G, Nogami M, Kityk I. Synthesis and characterization of anhydrous proton conducting inorganic–organic composite membranes for medium temperature proton exchange membrane fuel cells (PEMFCs). Energy. 2010;35:5260-8.
[12] Lin H-L, Yu TL, Chang W-K, Cheng C-P, Hu C-R, Jung G-B. Preparation of a low proton resistance PBI/PTFE composite membrane. Journal of power sources. 2007;164:481-7.
[13] Liu Z, Wainright JS, Litt MH, Savinell RF. Study of the oxygen reduction reaction (ORR) at Pt interfaced with phosphoric acid doped polybenzimidazole at elevated temperature and low relative humidity. Electrochimica Acta. 2006;51:3914-23.
[14] Zhai Y, Zhang H, Xing D, Shao Z-G. The stability of Pt/C catalyst in H3PO4/PBI PEMFC during high temperature life test. Journal of Power Sources. 2007;164:126-33.
[15] Prokop M, Kodym R, Bystron T, Drakselova M, Paidar M, Bouzek K. Degradation kinetics of Pt during high-temperature PEM fuel cell operation part II: Dissolution kinetics of Pt incorporated in a catalyst layer of a gas-diffusion electrode. Electrochimica Acta. 2020;333:135509.
[16] Bevilacqua N, George M, Galbiati S, Bazylak A, Zeis R. Phosphoric acid invasion in high temperature PEM fuel cell gas diffusion layers. Electrochimica Acta. 2017;257:89-98.
[17] Jha V, Hariharan R, Krishnamurthy B. A 3 dimensional numerical model to study the effect of GDL porosity on high temperature PEM fuel cells. International Journal of Heat and Mass Transfer. 2020;161:120311.
[18] Kongstein O, Berning T, Børresen B, Seland F, Tunold R. Polymer electrolyte fuel cells based on phosphoric acid doped polybenzimidazole (PBI) membranes. Energy. 2007;32:418-22.
[19] Ferng Y, Su A, Hou J. Parametric investigation to enhance the performance of a PBI-based high-temperature PEMFC. Energy conversion and management. 2014;78:431-7.
[20] Bergmann A, Gerteisen D, Kurz T. Modelling of CO poisoning and its dynamics in HTPEM fuel cells. Fuel Cells. 2010;10:278-87.
[21] Boaventura M, Sander H, Friedrich KA, Mendes A. The influence of CO on the current density distribution of high temperature polymer electrolyte membrane fuel cells. Electrochimica Acta. 2011;56:9467-75.
[22] Moçotéguy P, Ludwig B, Scholta J, Barrera R, Ginocchio S. Long Term Testing in Continuous Mode of HT-PEMFC Based H3PO4/PBI Celtec-P MEAs for μ-CHP Applications. Fuel Cells. 2009;9:325-48.

[23] Korsgaard AR, Nielsen MP, Kær SK. Part one: A novel model of HTPEM-based micro-combined heat and power fuel cell system. International Journal of Hydrogen Energy. 2008;33:1909-20.
[24] Arsalis A. Modeling and simulation of a 100 kWe HT-PEMFC subsystem integrated with an absorption chiller subsystem. International journal of hydrogen energy. 2012;37:13484-90.
[25] Özcan O, Akın AN. Thermodynamic analysis of methanol steam reforming to produce hydrogen for HT-PEMFC: an optimization study. International Journal of Hydrogen Energy. 2019;44:14117-26.
[26] Bayrak ZU, Kaya U, Oksuztepe E. Investigation of PEMFC performance for cruising hybrid powered fixed-wing electric UAV in different temperatures. International Journal of Hydrogen Energy. 2020;45:7036-45.
[27] Reddy EH, Jayanti S. Thermal management strategies for a 1 kWe stack of a high temperature proton exchange membrane fuel cell. Applied Thermal Engineering. 2012;48:465-75.
[28] Sasiwimonrit K, Chang W-C. Thermal management of high-temperature polymer electrolyte membrane fuel cells by using flattened heat pipes. Thermal Science. 2020:135-.
[29] Zenith F, Seland F, Kongstein OE, Børresen B, Tunold R, Skogestad S. Control-oriented modelling and experimental study of the transient response of a high-temperature polymer fuel cell. Journal of Power Sources. 2006;162:215-27.
[30] Andreasen SJ, Kær SK. Modelling and evaluation of heating strategies for high temperature polymer electrolyte membrane fuel cell stacks. International Journal of Hydrogen Energy. 2008;33:4655-64.
[31] Lotrič A, Sekavčnik M, Kuštrin I, Mori M. Life-cycle assessment of hydrogen technologies with the focus on EU critical raw materials and end-of-life strategies. International Journal of Hydrogen Energy. 2021;46:10143-60.
[32] Peng J, Lee SJ. Numerical simulation of proton exchange membrane fuel cells at high operating temperature. Journal of Power Sources. 2006;162:1182-91.
[33] Liu F, Kvesić M, Wippermann K, Reimer U, Lehnert W. Effect of spiral flow field design on performance and durability of HT-PEFCs. Journal of The Electrochemical Society. 2013;160:F892.
[34] Lobato J, Cañizares P, Rodrigo MA, Pinar FJ, Mena E, Úbeda D. Three-dimensional model of a 50 cm2 high temperature PEM fuel cell. Study of the flow channel geometry influence. International Journal of Hydrogen Energy. 2010;35:5510-20.
[35] Yin Y, Wang J, Yang X, Du Q, Fang J, Jiao K. Modeling of high temperature proton exchange membrane fuel cells with novel sulfonated polybenzimidazole membranes. International journal of hydrogen energy. 2014;39:13671-80.
[36] Drakselová M, Kodým R, Šnita D, Beckmann F, Bouzek K. Three-dimensional macrohomogeneous mathematical model of an industrial-scale high-temperature PEM fuel cell stack. Electrochimica Acta. 2018;273:432-46.
[37] Taccani R, Zuliani N. Effect of flow field design on performances of high temperature PEM fuel cells: experimental analysis. International Journal of hydrogen energy. 2011;36:10282-7.
[38] Tseng C-J, Heush Y-J, Chiang C-J, Lee Y-H, Lee K-R. Application of metal foams to high temperature PEM fuel cells. International journal of hydrogen energy. 2016;41:16196-204.
[39] Bandlamudi V, Bujlo P, Linkov V, Pasupathi S. The Effect of Potential Cycling on High Temperature PEM Fuel Cell with Different Flow Field Designs. Fuel Cells. 2019;19:231-43.
[40] Li X, Sabir I. Review of bipolar plates in PEM fuel cells: Flow-field designs. International journal of hydrogen energy. 2005;30:359-71.
[41] Song Y, Zhang C, Ling C-Y, Han M, Yong R-Y, Sun D, et al. Review on current research of materials, fabrication and application for bipolar plate in proton exchange membrane fuel cell. International Journal of Hydrogen Energy. 2020; 45(54)29832-29847.

[42] Wang X-D, Duan Y-Y, Yan W-M. Numerical study of cell performance and local transport phenomena in PEM fuel cells with various flow channel area ratios. Journal of Power Sources. 2007;172:265-77.
[43] Nam JH, Lee K-J, Sohn S, Kim C-J. Multi-pass serpentine flow-fields to enhance under-rib convection in polymer electrolyte membrane fuel cells: Design and geometrical characterization. Journal of Power Sources. 2009;188:14-23.
[44] Shimpalee S, Van Zee J. Numerical studies on rib & channel dimension of flow-field on PEMFC performance. International Journal of Hydrogen Energy. 2007;32:842-56.
[45] Kerkoub Y, Benzaoui A, Haddad F, Ziari YK. Channel to rib width ratio influence with various flow field designs on performance of PEM fuel cell. Energy Conversion and Management. 2018;174:260-75.
[46] Ni M, Shao ZP, Fuel cells that operate at 300º to 500ºC. Science. 2020, 369(6500)138-139.
[47] Ubong E, Shi Z, Wang X. Three-dimensional modeling and experimental study of a high temperature PBI-based PEM fuel cell. Journal of The Electrochemical Society. 2009;156:B1276.
[48] Reid RC, Prausnitz JM, Poling BE. The properties of gases and liquids. 1987.
[49] Chase Jr MW. NIST-JANAF thermochemical tables. J Phys Chem Ref Data, Monograph. 1998;9.
[50] Jiao K, Li X. A Three-Dimensional Non-isothermal Model of High Temperature Proton Exchange Membrane Fuel Cells with Phosphoric Acid Doped Polybenzimidazole Membranes. Fuel Cells. 2010;10:351-62.
[51] Coker AK. Appendix C: Physical properties of liquids and gases. Ludwig's Applied Process Design for Chemical and Petrochemical Plants. 2007;1:827-62.
[52] Braker W, Mossman AL. Matheson gas data book. 1971.
[53] Chen T-C, Lin W-J, Chen D-L. Effect of temperature gradient on simultaneously experimental determination of thermal expansion coefficients and elastic modulus of thin film materials. Journal of applied physics. 2004;96:3800-6.